Research
A SCIENCE PARTNER JOURNAL

RESEARCH ARTICLE

Insight into the Role and Evidence of Oxygen Vacancies in Porous Single-Crystalline Oxide to Enhance Catalytic Activity and Durability

Lingting Ye[1,2,3], Jiaming Ma[1,2,3], Jie Zhang[1,2,3], Wen Yin[4], Yuanguang Xia[4], and Kui Xie[1,2,3*]

[1]Key Laboratory of Optoelectronic Materials Chemistry and Physics, Fujian Institute of Research on the Structure of Matter, Chinese Academy of Sciences, Fuzhou, Fujian 350002, China. [2]Fujian Science & Technology Innovation Laboratory for Optoelectronic Information of China, Fuzhou, Fujian 350108, China. [3]Advanced Energy Science and Technology Guangdong Laboratory, 29 Sanxin North Road, Huizhou, Guangdong 116023, China. [4]Spallation Neutron Source Science Center, Dongguan, Guangdong 523803, China.

*Address correspondence to: kxie@fjirsm.ac.cn

Citation: Ye L, Ma J, Zhang J, Yin W, Xia Y, Xie K. Insight into the Role and Evidence of Oxygen Vacancies in Porous Single-Crystalline Oxide to Enhance Catalytic Activity and Durability. *Research* 2023;6:Article 0233. https://doi.org/10.34133/research.0233

Submitted 1 July 2023
Accepted 31 August 2023
Published 21 September 2023

Copyright © 2023 Lingting Ye et al. Exclusive licensee Science and Technology Review Publishing House. No claim to original U.S. Government Works. Distributed under a Creative Commons Attribution License 4.0 (CC BY 4.0).

Introducing and stabilizing oxygen vacancies in oxide catalysts is considered to be a promising strategy for improving catalytic activity and durability. Herein, we quantitatively create oxygen vacancies in the lattice of porous single-crystalline β-Ga_2O_3 monoliths by reduction treatments and stabilize them through the long-range ordering of crystal lattice to enhance catalytic activity and durability. The combination analysis of time-of-flight neutron powder diffraction and extended x-ray absorption fine structure discloses that the preferential generation of oxygen vacancy tends to occur at the site of tetrahedral coordination oxygen ions (O_{III} sites), which contributes to the formation of unsaturated Ga–O coordination in the monoclinic phase. The oxygen vacancies are randomly distributed in lattice even though some of them are present in the form of domain defect in the PSC Ga_2O_3 monoliths after the reduction treatment. The number of oxygen vacancies in the reduced monoliths gives 2.32×10^{13}, 2.87×10^{13}, and 3.45×10^{13} mg^{-1} for the $Ga_2O_{2.952}$, $Ga_2O_{2.895}$, and $Ga_2O_{2.880}$, respectively. We therefore demonstrate the exceptionally high C_2H_4 selectivity of ~100% at the C_2H_6 conversion of ~37% for nonoxidative dehydrogenation of C_2H_6 to C_2H_4. We further demonstrate the excellent durability even at 620 °C for 240 h of continuous operation.

Introduction

Oxygen vacancy (V_O)-associated defects are often considered as active sites that are composed of unsaturated coordination structures in oxide catalysts in catalytic reactions. The concentration of V_O in metal oxides is usually determined by the oxygen deficiency, which is normally dynamic and controlled by the properties of the electron orbitals of cations in the oxides [1–5]. Therefore, the V_O needs to be uniformly distributed and effectively stabilized in the crystal lattice. Creating V_O in the catalysts would highly facilitate the catalytic activity, while stabilizing the V_O would improve the durability of catalysts [6,7].

β-Ga_2O_3 is a highly efficient catalyst that is usually used for light alkane dehydrogenation reaction [8,9]. β-Ga_2O_3 is a monoclinic *n*-type semiconductor with the space group of C_2/m and the lattice parameters *a*, *b*, *c*, and *β* of 12.23 Å, 3.04 Å, 5.80 Å, and 103.7°, respectively [10,11]. The unit cell consists of 2 Ga ions and 3 types of O ions that are located in the tetrahedral and octahedral coordination, respectively. Two O ions have a triple coordination, and the third O has a tetrahedral coordination. Due to the unique feature of electron orbital of Ga, the β-Ga_2O_3 is chemically and thermally stable especially at reduced temperatures. Reduction treatment produces V_O in β-Ga_2O_3 at a certain temperature, which creates the low-coordinated Ga active sites in the electron-deficient surface. It has been confirmed that these active sites markedly facilitate the enhancement of catalytic activity of nonoxidative C_2H_6 dehydrogenation, especially for the C–H activation, but avoid the C–C bond breakage at reduced temperatures [12–14]. C_2H_4 is the most widely used block material in the manufacture of polymers and other chemicals [15,16]. Although the β-Ga_2O_3 with oxygen deficiency is highly active [17,18], the activity is only observed at the initial stage because the agglomeration of oxygen defects tends to produce amorphous layers at surface that blocks the active site and degrades the catalytic activity in reactions.

Porous single-crystalline β-Ga_2O_3 (PSC Ga_2O_3) monoliths at the macroscale incorporates the synergistic effect of interconnected pores and single-crystalline skeleton in the porous architectures, which yields both long-range ordered and well-defined structures of the lattice in the materials [19,20]. The interconnected pores facilitate the rapid diffusion of species and provide a large surface area for chemical reactions. The long-range

ordering of the lattice offers a unique path for creating and stabilizing the V_O in lattice in the interconnected single-crystalline skeletons in the porous architecture. Therefore, PSC Ga_2O_3 monoliths at the macroscale would combine the long-range ordering of the lattice and the disordering of the interconnected pores, thereby improving the properties of the materials themselves. These structures have inherent mechanical and thermal stability, facilitate the species diffusion through 3-dimensional percolation, and are easy to process into complex structures. The monoliths would therefore have the advantages of high catalytic performance and thermal durability in the catalytic reactions [21].

Herein, we fabricate PSC Ga_2O_3 monolith and engineer the oxygen deficiency in lattice to create active sites associated with oxygen vacancies on the well-defined surface in the porous architectures. We further correlate the concentration of V_O with catalytic performance. As a case study, we demonstrate the exceptionally high performance of nonoxidative dehydrogenation of C_2H_6 to C_2H_4 with excellent durability during the continuous operation of 240 h.

Results

PSC Ga_2O_3 monoliths are grown from the mother phase of $GaPO_4$ single crystal by a lattice reconstruction strategy in a solid-solid transformation process. The growth mechanism is demonstrated in Figs. S1 and S2, which indicates a lattice channel of P/O atoms. The lattice mismatch between β-Ga_2O_3 and $GaPO_4$ would dominate the preferential growth of facet in the porous architectures. The porosity is ~66% for PSC Ga_2O_3 monoliths, which is favorable for the species diffusion through the 3-dimensional percolation. The x-ray diffraction (XRD) patterns of the PSC Ga_2O_3 monoliths with (100) and (001) facets are grown from $GaPO_4$ with (−132) and (012) facets, respectively. Figure 1A and Fig. S3 display the microstructures of the PSC Ga_2O_3 monoliths. It is shown that the uniform pore size distribution is at ~100 nm. In Fig. S4, Brunauer–Emmett–Teller test further reveals the pore size of ~110 to 130 nm and specific surface area of ~5 m^2/g. Figure 1B and Fig. S5 show scanning transmission electron microscopy (STEM) and selected area electron diffraction (SAED) images of the PSC Ga_2O_3 monoliths,

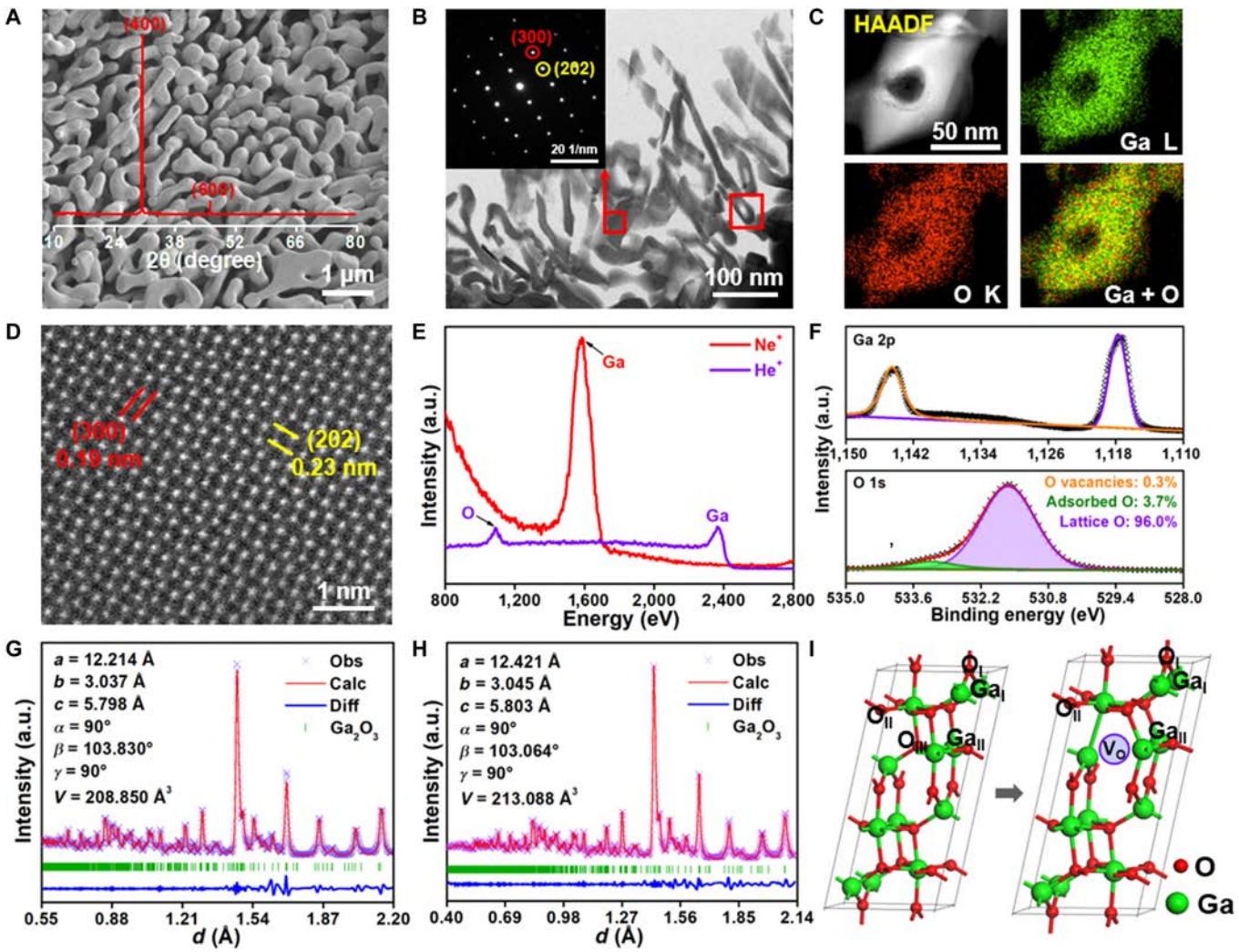


Fig. 1. Microstructure of PSC Ga_2O_3 monoliths. (A) Scanning electron microscopy and XRD patterns of PSC Ga_2O_3 monoliths. (B to D) Scanning transmission electron microscopy, SAED, high-angle annular dark-field (HAADF), element mapping, and Cs-HRTEM of PSC Ga_2O_3 monoliths with the face of (100). (E and F) HS-LEISS and XPS of the PSC Ga_2O_3 monoliths. (G and H) Observed (crosses), calculated (solid line), and differential TOF NPD patterns of PSC Ga_2O_3 powder. (I) Crystal structures of β-Ga_2O_3 from TOF NPD datasets. a.u., arbitrary units.

respectively. The porous architecture is pretty uniform with interconnected single-crystalline skeletons. The high-angle annular dark-field image and elemental mappings in Fig. 1C show that the Ga and O are evenly distributed in the skeleton. We have only observed the presence of Ga and O elements in the samples, further proving that the P element is absent, indicating the complete conversion of $GaPO_4$ to Ga_2O_3 in Fig. S6. The P element has been completely removed during the process by transforming the mother phase of $GaPO_4$ single crystal into PSC Ga_2O_3 monolith. In addition, the element mapping indicates the absence of element separation in the skeletons. In Fig. 1D, the spherical aberration-corrected high-resolution transmission electron microscopy (Cs-HRTEM) shows the lattice spacings of 0.19 and 0.23 nm, which indicates the good reference to (300) and (202) facets, respectively.

In Fig. 1E and Fig. S7, the high-sensitivity low-energy ion scattering spectra (HS-LEISS) show that the PSC Ga_2O_3 monoliths exhibit the presence of Ga and O on the top layer, forming a series of clear Ga–O coordination structures on the surfaces. According to x-ray photoelectron spectroscopy (XPS) in Fig. 1F and Fig. S8, the oxidation states of Ga and O are +3 and −2, respectively. The ratio of O vacancies calculated from the peak area is only 0.3% to 0.4%, which indicates that the O vacancies can be basically ignored in the pristine PSC Ga_2O_3 monoliths. Time-of-flight neutron powder diffraction (TOF NPD) in Fig. 1G and H indicates that the PSC Ga_2O_3 powder could be indexed assuming a monoclinic with space group C1 2/m. Selected atomic spacings, corresponding to the coordination refined from TOF NPD data, are used to draw the corresponding structure in Fig. 1I. Ga_2O_3 has 2 coordination structures, tetrahedral coordination site (Ga(t)) and octahedral one (Ga(o)). In β-Ga_2O_3 phase, the ratio of Ga(t) to Ga(o) is known as 1:1 [22,23]. The preferential generation of V_O tends to occur in the tetrahedral coordination oxygen ions (O_{III} sites), which contributes to the unsaturated Ga–O coordination in the monoclinic phase. This suggests that the active sites tend to be produced at the Ga(t) and further indicates that the catalytic activity of oxygen vacancies located in Ga(t) is superior to that in Ga(o).

Figure 2A and B and Figs. S9 and S10 show the formation of different concentration of V_O in lattice, which indicates that the V_O can be isolated even at the concentration of as high as up to 14%. We show detailed information on the density of states of β-Ga_2O_3 with different V_O concentrations. We can observe that the valence band is mainly made up of the O 2p state with a small amount of the Ga 4p state. The local electronic structure of β-Ga_2O_3 also changes with the emergence of V_O [24]. Moreover, the main changes occur in the valence state of oxygen 2p state, and the band gap width of β-Ga_2O_3 with different V_O concentrations becomes narrower compared to pure β-Ga_2O_3. We create the different concentrations of V_O in lattice by directly reducing the PSC Ga_2O_3 monoliths and oxidize the reduced samples by using thermal gravimetric analysis to determine their chemical formula to be $Ga_2O_{2.952}$, $Ga_2O_{2.895}$, and $Ga_2O_{2.880}$, respectively, in Fig. S11. We observe that the XRD of PSC Ga_2O_3 monoliths are slightly shifted to a low angle after reduction, indicating that the introduction of a large number of oxygen vacancies may cause the lattice expansion in Fig. S12A. Nevertheless, no phase transition is observed in the β-Ga_2O_3 even after the high temperature treatment in a reducing gas, firmly verifying the excellent thermal stability of the PSC Ga_2O_3 monoliths. The SAED image of PSC $Ga_2O_{2.880}$ monoliths reveals that it is a monoclinic structured β-Ga_2O_3 single crystal with the (100) facet in Fig. S12B, which is consistent with the XRD result. HS-LEISS is used to identify the ratio between O and Ga at the top layer in Fig. S13, which further confirms the changes in surface oxygen concentration from ~25.3% to ~24.8%. Electron spin resonance (ESR) results as shown in Fig. 2C and Fig. S14 further confirm the existence of V_O. The 3 reduced PSC Ga_2O_3 monoliths all show pairs of steep peaks and symmetric distributions at $g = 2.003$, indicating that electrons are trapped in the V_O [25]. In addition, we further quantify the number of V_O in the reduced PSC Ga_2O_3 monoliths, which gives 2.32×10^{13}, 2.87×10^{13}, and 3.45×10^{13} mg^{-1} for the $Ga_2O_{2.952}$, $Ga_2O_{2.895}$, and $Ga_2O_{2.880}$, respectively.

Indirect evidence in Cs-HRTEM is usually utilized to assist the proof of the presence of V_Os especially in domain defects in oxide samples [25,26]. We tentatively conduct the structural analysis based on Cs-HRTEM image to visualize possible defects induced in the samples. The disordered Ga atoms in the form of bright dots in the domain in the size of ~1 to 2 nm have been observed in the bright-field Cs-HRTEM image in Fig. 2D with the inset as marked with an ellipse in the line profile. This may be mainly attributed to the loss of oxygen in lattice that contributes to the formation of domain defects. In contrast, the disordered white clusters that represent O atoms in the domain in the size of ~1 to 2 nm have been observed in the dark-field Cs-HRTEM image in Fig. 2E, which is possibly attributed to the loss of lattice oxygen in the sample, whereas the corresponding domain as marked with an ellipse in the dark-field Cs-HRTEM image in Fig. 2E possesses disordered Ga atoms possibly blocked by V_O defects in the light-field Cs-HRTEM image in the inset. We have added more data to verify the prevalence of domain defects with V_O in Cs-HRTEM images in Fig. S15. This indicates that a large number of oxygen vacancies are randomly distributed in the domain defects in the sample after the high-temperature treatment in a reducing gas. Although the V_O is isolated according to theory calculation, we still observe the slight agglomeration of V_O in lattice. However, the $Ga_2O_{2.880}$ still maintains the single-crystalline features, to well stabilize the V_O in the lattice.

To further understand the local structural differences of the PSC Ga_2O_3 monoliths with or without V_O, systematic Ga *K*-edge extended x-ray absorption fine structure (EXAFS) data are studied by applying Athena-Artemis software in Fig. 2F and Figs. S16 and S17 [27–29]. We observe that there is no phase transformation with or without V_O in the PSC Ga_2O_3 monoliths, and the β-Ga_2O_3 phase is still identified [30,31]. It can be seen that the model well fits with the experimental data. The *R*-factor is <0.2% in the fitting results with all samples. Actually, the slight variation of coordination number is quite negligible for Ga–O and Ga–Ga of the samples even after reduction because the change of oxygen nonstoichiometry is quite small in $Ga_2O_{3-\delta}$. Therefore, it is a usual way to fit the EXAFS data by fixing the coordination number of Ga–O in GaO_4 tetrahedra and GaO_6 octahedra at 4 and 6, respectively. All samples are likely to have 1 oscillation in the Ga–O shell. From the fit, the Ga–O bond length is gradually shortened from 1.882 to 1.747 Å for the samples after reduction. Moreover, it is observed that the Ga–Ga bond length is slightly shortened from 3.206 to 3.202 Å for the sample after reduction. We have added the O *K*-edge EXAFS of PSC Ga_2O_3 monoliths before and after reduction in Fig. S18. The O *K*-edge spectrum is divided into 2 regions. The first region is between 533 and 544 eV and possesses 2 broad absorption bands. Peaking at 537 and 542.8 eV, respectively, these 2 features arise mainly due to

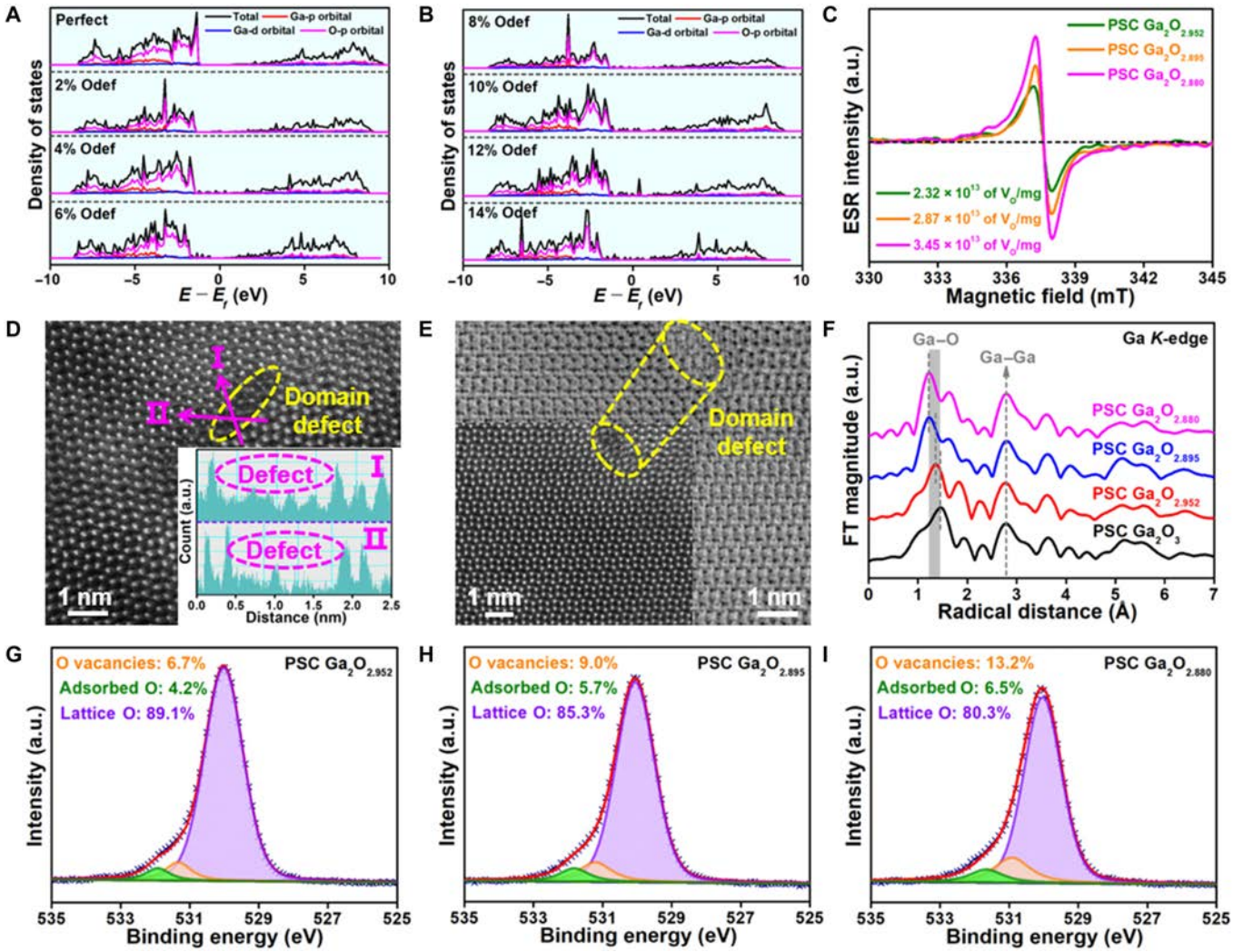


Fig. 2. Oxygen vacancies in PSC Ga_2O_3 monoliths. (A and B) Density of states of β-Ga_2O_3 with different concentrations of V_Os. (C) ESR spectra of the 3 reduced PSC Ga_2O_3 monoliths. (D and E) Cs-HRTEM images with different area of the PSC $Ga_2O_{2.880}$ monoliths. (F) Fourier transforms (FT) derived from EXAFS oscillations with different samples. (G to I) XPS of O 1s in the 3 reduced PSC Ga_2O_3 monoliths.

the excitation of O 2p–Ga 4s and O 2p–Ga 4p hybridization orbitals. These 2 polarized peaks tend to shift to lower energies with deeper reduction, and the peaks become shorter due to the shorter bond lengths of the Ga–O bonds. The second region is an EXAFS pseudo-oscillation produced by the multiple scattering effect of the O element with the surrounding metallic elements. This result indicates that V_O can exist stably in reduced PSC Ga_2O_3 monoliths, and these active structures are beneficial for improving dehydrogenation activity and carbon deposition resistance. In Fig. 2G to I and Fig. S19, the XPS results of the O 1s states of the PSC Ga_2O_3 monoliths after reduction indicates the changing trends of the concentration of V_O at surface. Three peaks of oxygen species, fitted from Gaussian simulation, can be attributed to lattice oxygen, oxygen vacancies, and adsorbed oxygen. The chemical state of Ga 2p remains basically unchanged of the 3 reduced PSC Ga_2O_3 monoliths. However, the binding energy of Ga 3d is 19.7 eV in XPS of PSC $Ga_2O_{2.880}$ monoliths after reduction. In contrast, the binding energy of Ga 3d is 19.5 eV in the XPS of PSC Ga_2O_3 monoliths before reduction. It can be seen that the binding energy of Ga 3d increases slightly with the increase of the concentration of oxygen defect in lattice. This suggests that the Ga–Ga bond is slightly strengthened, which is consistent with the EXAFS result.

We further utilize ambient-pressure XPS (AP-XPS) in Shanghai Synchrotron Radiation Facility to analyze the chemical changes of Ga and O at surface in the PSC $Ga_2O_{2.880}$ monolith under reaction conditions [32,33]. Figure 3A to C shows the spectra of Ga 2p and O 1s of the catalyst in pure ethane from 600 to 660 °C. With increasing temperature, the binding energy of Ga 2p gradually increases by up to ~0.9 eV, indicating that the interaction force of the Ga–Ga bond is strengthened. The asymmetric peak of O 1s in Fig. 3C can be broken into 2 peaks by Gaussian fitting. The stronger peak is attributed to the oxygen in the reduced PSC Ga_2O_3, and the weaker peak is attributed to the C/O species adsorbed on the surface. The binding energy of O 1s is ~1.0 eV higher under a temperature range of 600 to 660 °C, indicating that the higher the temperature is, the easier it is to adsorb C_2H_6 molecules. We then utilize in situ Fourier transform infrared (FTIR) spectroscopy to survey the activation process of C_2H_6 in the PSC $Ga_2O_{2.880}$ monoliths in Fig. 3D to F. With increasing temperature, the

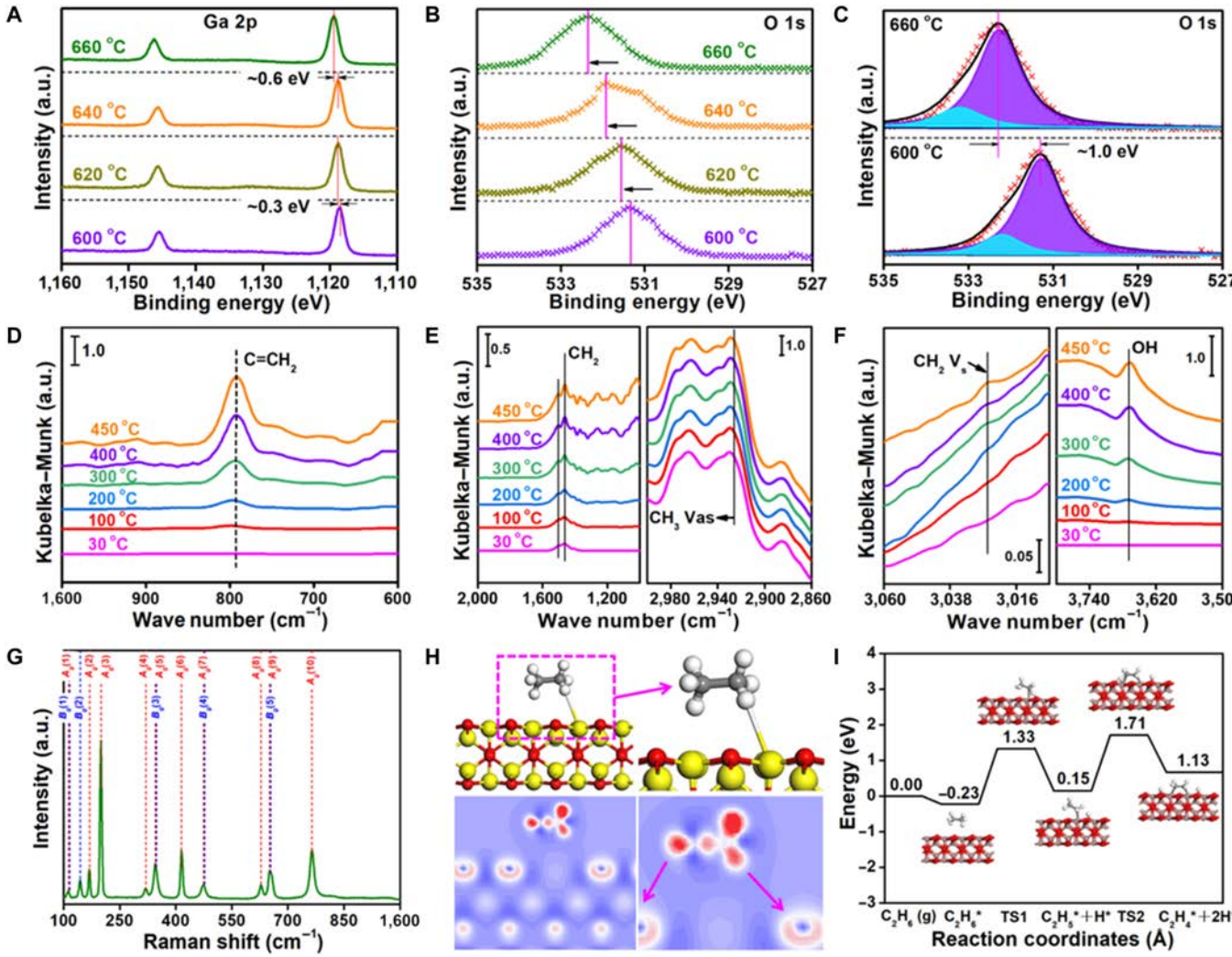


Fig. 3. Mechanism of catalysis toward nonoxidative ethane dehydrogenation. (A to C) AP-XPS spectra of Ga 2p and O 1s under different temperatures. (D to F) In situ FTIR of the PSC $Ga_2O_{2.880}$ monoliths under different temperatures. (G) In situ Raman spectra of the PSC $Ga_2O_{2.880}$ monoliths at room temperature. (H) The activation process (top) and electron transfer (bottom) of β-Ga_2O_3 for ethane. (I) Potential energy of ethane dehydrogenation on β-Ga_2O_3 surface containing oxygen vacancies (gray is carbon, white is hydrogen, brown is gallium, and red is oxygen).

asymmetric stretching vibration of the C–H bond in ethane is obviously shifted to the blue region, indicating that the C–H bond is effectively activated to a higher energy state. Additionally, the stretching vibrations of the C–H and C=C bonds of C_2H_4 become increasingly obvious, suggesting that the initial temperature of C_2H_6 dehydrogenation to C_2H_4 in the β-Ga_2O_3 phase is as low as ~200 °C. The CH_2, $C{=}CH_2$, and OH are the intermediates in the process of the nonoxidative dehydrogenation from C_2H_6 to C_2H_4 [34].

Information about the symmetry of the crystal structures is obtained by the Raman analysis, which indicates the monoclinic structure of β-Ga_2O_3. It consists of a tetrahedron structure (Ga_IO_4) and an octahedron structure ($Ga_{II}O_6$) and includes 2 categories of Ga atoms (Ga_I and Ga_{II}) and 3 categories of O atoms (O_I, O_{II} and O_{III}) in Fig. S20. We utilize in situ Raman spectra to survey the phase transition of C_2H_6 in the PSC $Ga_2O_{2.880}$ monoliths in Fig. 3G. The Raman peak confirms that no phase transition occurred [35]. Figure S21 shows the FTIR spectroscopy of adsorbed pyridine for distinguishing between a Lewis acid and Bronsted acid. The absence of Bronsted acid in the β-Ga_2O_3 phase is indicated by the absence of a characteristic absorption band at ~1,540 cm^{-1}. Figure 3H shows the configuration of chemisorption of C_2H_6 at surface, which indicates that the electrons are transferred from H to Ga atoms in the configurations. Figure 3I shows the process (C_2H_6 (g) → C_2H_6* → C_2H_5* + H* → C_2H_4* + 2H*) and the density functional theory (DFT)–calculated potential energy for the direct dehydrogenation of C_2H_6. The adsorption energy (Eads) of the C_2H_6 molecule is −0.23 eV, and the energy barrier is 1.56 eV for each elementary process. Reasonable activation energies and potential energy barriers indicate that the adsorbed C_2H_6 molecules can be efficiently activated, and the C–H bond cleavage tends to convert C_2H_6 to C_2H_4.

Figure 4A and Fig. S22 display the product analysis for the nonoxidative dehydrogenation from C_2H_6 to C_2H_4. We discover that the ethylene is a dominant product and that the methane exists as a by-product. This result suggests a carbon balance of ~100% in Fig. 4B, further indicating that there is no carbon deposition during the reaction. The well-defined surfaces coupled with tailored V_O effectively improve the activation of C–H

bonds in C_2H_6 and coking resistance. Figure 4C and D and Fig. S23 display the C_2H_6 conversion and C_2H_4 selectivity during the nonoxidative dehydrogenation process. C_2H_6 conversion on PSC $Ga_2O_{2.880}$ monoliths gradually increase versus temperature and finally reaches ~37% at 660 °C. In the control experiment, it is ~5 times higher than that of the thermal cracking of C_2H_6 without catalyst. The C_2H_4 selectivity of the PSC $Ga_2O_{2.880}$ monoliths can be up to ~100%. That of the control experiment is much higher than the ethylene selectivity of the thermal cracking of C_2H_6 without a catalyst. Here, the well-defined surfaces coupled with tailored V_O are considered to be active sites for the dehydrogenation of C_2H_6. The property of the active site governs the difference in the catalytic conversion and selectivity for dehydrogenating C_2H_6 to C_2H_4. In addition, the C_2H_6 dehydrogenation of different samples is performed at 620 °C, and stable C_2H_6 conversion and C_2H_4 selectivity are shown in Fig. 4E and F without degradation after 240 h of operation. We have added the characterization of the catalysts after the stability test for the dehydrogenation of C_2H_6 at 620 °C in Fig. S24. The XRD patterns confirm the structural stability of the 3 reduced PSC Ga_2O_3 monoliths after the stability test. The chemical states of Ga and O remain basically unchanged after the stability test. The Raman spectra confirm no visible coke formation after the stability test. In addition, the microstructure of the PSC $Ga_2O_{2.880}$ monoliths generally remain unchanged after stability test in Fig. S25. The domain defects associated with oxygen vacancies are not increased in lattice, which also reveals the excellent structural stability of PSC $Ga_2O_{2.880}$ monolith.

In order to further validate the stability, we conduct in situ spectroscopy to understand the surface states of the PSC $Ga_2O_{2.880}$ monoliths during the reaction. In Fig. 4G, we perform in situ Raman scattering studies of the PSC $Ga_2O_{2.880}$ monoliths from 0 to 100 h in pure C_2H_6 and find that the crystal structure remains stable without any visible change. In addition, we also find no obvious coke formation during the 100-h test. We perform in situ HS-LEISS spectra of the PSC $Ga_2O_{2.880}$ monoliths from 0 to 50 h in pure C_2H_6 in Fig. 4H. The compositions of Ga and O at the top layers remain essentially constant, and there is no carbon peak on the surface, indicating that the PSC $Ga_2O_{2.880}$ monoliths can exist stably under pure C_2H_6 at high temperature. These results indicate that the well-defined surfaces of the PSC Ga_2O_3 monoliths can accommodate oxygen vacancies, thus stabilizing

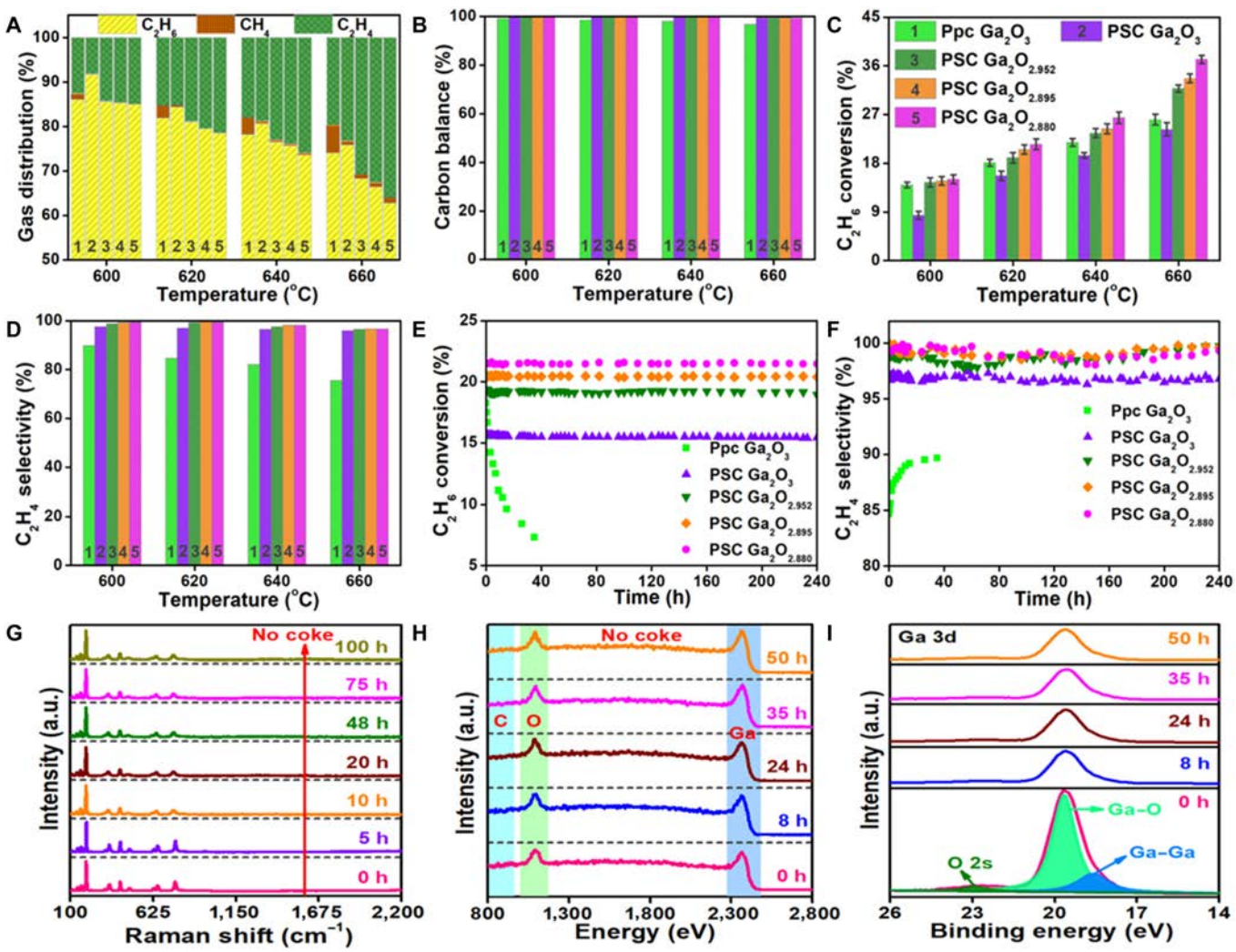


Fig. 4. Nonoxidative ethane dehydrogenation to ethylene. (A to D) Product analysis, carbon balance, ethane conversion, and ethylene selectivity with different samples. (E and F) Long-term stability of ethane dehydrogenation at 620 °C. (G to I) In situ Raman, in situ HS-LEISS, and in situ XPS of the PSC $Ga_2O_{2.880}$ monoliths in pure ethane. Ppc Ga_2O_3 stands for porous polycrystalline β-Ga_2O_3.

the crystal structure and improving the carbon deposition resistance. Figure 4I presents the in situ XPS spectra of the PSC $Ga_2O_{2.880}$ monoliths after 0 to 50 h of reaction in pure C_2H_6. The binding energy peaks of Ga 3d at 22.96, 19.65, and 18.59 eV are visible, which originates from the O 2s, Ga–O, and Ga–Ga bonds of the reduced PSC Ga_2O_3, respectively. Moreover, the Ga 3d peak intensity is not visibly changed with increasing reaction time.

Conclusion

In summary, we quantitatively introduce V_Os and stabilize them by the long-range ordering of crystal lattice in a centimeter-scale PSC Ga_2O_3 monolith to boost the catalytic activity and durability. The oxygen vacancies are well stabilized in lattice even with slight agglomeration into domain defects ~1 to 2 nm at a high oxygen deficiency. The formation of low-coordinated Ga active sites therefore delivers an exceptionally high C_2H_4 selectivity of ~100% at an C_2H_6 conversion of ~37% even only at 660 °C for the nonoxidative dehydrogenation of C_2H_6 to C_2H_4. We have further demonstrated the outstanding stability in a continuous operation of up to 240 h. This work would not only facilitate the rational design of catalytic materials but also find potential applications of the porous single crystals in other fields.

Materials and Methods

Synthesis

We grew single-crystalline $GaPO_4$ using the Bridgman method and cut it into (-132) and (012) substrates to grow porous single crystals. We treated the single-crystalline $GaPO_4$ substrates at ~100 to 400 Torr (pure Ar) for 50 h at ~1,100 to 1,300 °C to grow PSC Ga_2O_3 monoliths. The flow rate of pure Ar was ~100 to 500 sccm, and then the crystals were slowly cooled to room temperature under a slow flow of pure Ar. We constructed oxygen vacancies in the PSC Ga_2O_3 monoliths by heat treatment with a reducing gas (5% H_2/95% Ar) at 700 °C for ~5 to 20 h. The gas flow rate is 50 ml min^{-1}.

Characterization

The crystalline structure of samples was characterized by using XRD (Cu-Ka, Empyrean, Panalytical). The microstructures, morphologies, and elemental analysis of the samples were analyzed by using a field emission scanning electron microscope (FE-SEM) and EDS (SU-8010). TOF NPD was collected on the general-purpose powder diffractometer with a 360° rotation stage at China Spallation Neutron Source. The TOF NPD datasets were determined by Rietveld refinement performed on a crystallography data analysis software GSAS-II. Brunauer–Emmett–Teller test was conducted using a porosity analyzer (Tristar II 3020). The lattice structures, SAED patterns, and elemental mapping of the samples were analyzed using Cs-TEM (FEI Titan3 G2 60-300). Focused ion beam nanotomography (Hellos 650, Zeiss Auriga) was performed to obtain TEM slices with porous ultrathin microstructures. The composition of the top layer of the sample was examined by HS-LEISS (Otac100, ION-TOF). The Ga *K*-edge EXAFS was collected at the 21A x-ray nanodiffraction beamline of Taiwan Photon Source, National Synchrotron Radiation Research Centre, with photon fluxes on the sample ranging from 1×10^{11} to 3×10^9 photons per second and x-ray energies of 6 to 27 KeV. The O *K*-edge EXAFS was executed by the 4W7B of Beijing Synchrotron Radiation Facility (BSRF). The operating voltage of the BSRF storage ring is 2.5 GeV, and the average current is 250 mA. The chemical states of elements were determined by XPS (ESCALAB 250Xi). Thermal gravimetric analysis was conducted using a Netzsch STA449F3 to calculate oxygen nonstoichiometry. Raman (HR800 Evolution, Horiba) was used to analyze the samples. ESR (E500, Bruker-BioSpin) was used to confirm the existence of oxygen vacancies. Near AP-XPS experiment was performed at the beamline BL02B01 of Shanghai Synchrotron Radiation Facility. In situ FTIR measurement was carried out using an IR spectrometer (Bruker VERTEX 70).

Catalytic test

Catalytic tests were carried out under atmospheric pressure using the tube reaction system, which had a flow quartz microreactor with an inner diameter of 3 mm. For the dehydrogenation of C_2H_6, the gas reactants contained 10 vol% C_2H_6 and 90 vol% Ar. The flow rate of the gas reactant was 5 ml min^{-1}. The reaction products were analyzed using an online gas chromatograph (GC2014, Shimazu, Japan) equipped with a flame ionization detector (FID) and a thermal conductivity detector (TCD) and a 30-m packed column of CP-poraplot Q.

Theoretical calculations

Spin-polarized DFT calculations were carried out a periodic slab model using Vienna Ab initio Simulation Package. The electron–ion interaction was clearly defined by the projected augmented wave pseudopotential with a plane wave cutoff of 500 eV. The generalized gradient approximation, including Perdew–Burke–Ernzerhof, was applied to display the exchange and correlation functional throughout the calculations, which provided an efficient method for calculating the energies of all intermediates and transition states (TSs). During geometry optimization, 10^{-5} eV and 0.01 eV $Å^{-1}$ were used for convergence of the energies and residual forces. The β-Ga_2O_3 unit cell was calculated on a $3 \times 10 \times 6$ k-point grid, and the optimized lattice parameters were $a = 12.502$ Å, $b = 3.099$ Å, and $c = 5.912$ Å. To avoid the low-layer interaction with the periodic image, a vacuum gap of 20 Å was set up for a p (4×2) superstructure of the β-Ga_2O_3 (100) surface, where the bottom 5 layers of the atoms were frozen, the top 5 layers were fully relaxed, and a $3 \times 3 \times 1$ k-point grid was applied for Brillouin zone sampling. We used the climbing image nudged elastic band method to calculate the minimum reaction path for the C−H bond cleavage process and obtained the initial TS structure, which was subsequently used in Henkelman's dimer method to identify the final TS, and each TS had only 1 imaginary frequency. The adsorption energy and activation barrier were calculated by $E_{ads} = E_{adsorbate/sur} - E_{adsorbate} - E_{sur}$, $E_T = E_{TS} - E_{IS}$, where $E_{adsorbate/sur}$ is the total energy of surface and adsorbed ethane, $E_{adsorbate}$ is the energy of a single ethane molecule, E_{sur} is the energy of the free surface, E_{TS} is the energy of the TS structure, and E_{IS} is the energy of the initial state of the reactant.

Acknowledgments

We thank the beamline 4W7B at BSRF and technical assistance.
Funding: We acknowledge the Natural Science Foundation of China (22325506, 22379147, 22002167, 22101282, and 2227-9142), the Youth Innovation Promotion of Chinese Academy of Sciences (2023318), and the Natural Science Foundation of

Fujian Province (2020J05082 and 2020J01113). **Author contributions:** K.X. conceived and supervised the research. L.Y. and J.M. designed and performed the experiments. J.Z. conducted the DFT calculations. All authors discussed the results and commented on the manuscript. **Competing interests:** The authors declare that they have no competing interests.

Data Availability

The data used to support the findings of this study are available from the corresponding author upon request.

Supplementary Materials

Figs. S1 to S25

References

1. Xu Y, Wang X, Yang D, Tang Z, Cao M, Hu H, Wu L, Liu L, Mcleod J, Lin H, et al. Stabilizing oxygen vacancies in ZrO_2 by Ga_2O_3 boosts the direct dehydrogenation of light alkanes. *ACS Catal*. 2021;11(16):10159–10169.
2. Liu Y, Peng Y, Naschitzki M, Gewinner S, Schçllkopf W, Kuhlenbeck H, Pentcheva R, Cuenya BR. Surface oxygen vacancies on reduced Co_3O_4(100): Superoxide formation and ultra-low-temperature CO oxidation. *Angew Chem Int Ed*. 2021;60(30):16514–16520.
3. Peng B, Lu Q, Wang Y, Li J, Zhang Q, Huang H, Liu L, Li C, Zheng L, Wang Z. B-site nanoscale-ordered structure enables ultra-high tunable performance. *Research (Wash D C)*. 2022;2022:Article 9764976.
4. Ren W, Mei Z, Zheng S, Li S, Zhu Y, Zheng J, Lin Y, Chen H, Gu M, Pan F. Wavelength-dependent solar N_2 fixation into ammonia and nitrate in pure water. *Research (Wash D C)*. 2020;2020:Article 3750314.
5. Meng F, Zhang Q, Gao A, Liu X, Zhang J, Peng S, Lu X, Gu L, Li H. Synergistic O^{2-}/Li^+ dual ion transportation at atomic scale. *Research (Wash D C)*. 2019;2019:Article 9087386.
6. Xi S, Zhang J, Xie K. Low-temperature water-gas shift reaction enhanced by oxygen vacancies in Pt-loaded porous single-crystalline oxide monoliths. *Angew Chem Int Ed*. 2022;61(39):Article e202209851.
7. Pfisterer JHK, Liang Y, Schneider O, Bandarenka AS. Direct instrumental identification of catalytically active surface sites. *Nature*. 2017;549(7670):74–77.
8. Chen H, Gao P, Liu Z, Liang L, Han Q, Wang Z, Chen K, Zhao Z, Guo M, Liu X, et al. Direct detection of reactive gallium-hydride species on the Ga_2O_3 surface *via* solid-state NMR spectroscopy. *J Am Chem Soc*. 2022;144(38):17365–17375.
9. Matveyeva AN, Omarov SO, Sladkovskiy DA, Murzin DY. Experimental studies and kinetic regularities of Isobutane dehydrogenation over Ga_2O_3/Al_2O_3. *Chem Eng J*. 2019;372:1194–1204.
10. Liu J, Zhang Z, Jiang Y, Jiang X, He N, Yan S, Guo P, Xiong G, Su J, Vilé G. Influence of the zeolite surface properties and potassium modification on the Zn-catalyzed CO_2-assisted oxidative dehydrogenation of ethane. *Appl Catal B Environ*. 2022;304:Article 120947.
11. Liu T, Feng Z, Li Q, Yang J, Li C, Dupuis M. Role of oxygen vacancies on oxygen evolution reaction activity: β-Ga_2O_3 as a case study. *Chem Mater*. 2018;30(21):7714–7726.
12. Riley CR, De La Riva A, Ibarra IL, Datye AK, Chou SS. Achieving high ethylene yield in non-oxidative ethane dehydrogenation. *Appl Catal A Gen*. 2021;624:Article 118309.
13. Maeno Z, Yasumura S, Wu X, Huang M, Liu C, Toyao T, Shimizu KI. Isolated indium hydrides in CHA zeolites: Speciation and catalysis for nonoxidative dehydrogenation of ethane. *J Am Chem Soc*. 2020;142(10):4820–4832.
14. Pan Y, Bhowmick A, Wu W, Zhang Y, Diao Y, Zheng A, Zhang C, Xie R, Liu Z, Meng J, et al. Titanium silicalite-1 nanosheet-supported platinum for non-oxidative ethane dehydrogenation. *ACS Catal*. 2021;11(15):9970–9985.
15. Liu Y, Chen Y, Jiang W, Kong T, Camargo P, Gao C, Xiong Y. Highly efficient and selective photocatalytic nonoxidative coupling of methane to ethylene over Pd-Zn synergistic catalytic sites. *Research (Wash D C)*. 2022;2022:Article 9831340.
16. Huang H, Zhang N, Xu J, Xu Y, Li Y, Lü J, Cao R. Photocatalytic CO_2–to–ethylene conversion over Bi_2S_3/CdS heterostructures constructed via facile cation exchange. *Research (Wash D C)*. 2022;2022:Article 9805879.
17. Chang Q, Wang K, Sui Z, Zhou X, Chen D, Yuan W, Zhu Y. Rational design of single-atom-doped Ga_2O_3 catalysts for propane dehydrogenation: Breaking through volcano plot by Lewis acid−base interactions. *ACS Catal*. 2021;11(9):5135–5147.
18. Tang J, Lambie S, Meftahi N, Christofferson AJ, Yang J, Ghasemian MB, Han J, Allioux FM, Rahim MA, Mayyas M, et al. Unique surface patterns emerging during solidification of liquid metal alloys. *Nat Nanotechnol*. 2021;16(4):431–439.
19. Xiao Y, Li H, Xie K. Activating lattice oxygen at the twisted surface in a mesoporous CeO_2 single crystal for efficient and durable catalytic CO oxidation. *Angew Chem Int Ed*. 2021;60(10):5240–5244.
20. Cheng F, Duan X, Xie K. Dry reforming of CH_4/CO_2 by stable Ni nanocrystals on porous single-crystalline MgO monoliths at reduced temperature. *Angew Chem Int Ed*. 2021;60(34):18792–18799.
21. Yu X, Cheng F, Duan X, Xie K. Porous single-crystalline monolith to enhance catalytic activity and stability. *Research (Wash D C)*. 2022;2022:Article 9861518.
22. Cramer SP, Eccles TK, Kutzler FW, Hodgson KO, Mortenson LE. Molybdenum X-ray absorption edge spectra: The chemical state of molybdenum in nitrogenase. *J Am Chem Soc*. 1976;98(5):1287–1288.
23. Akatsuka M, Yoshida T, Yamamoto N, Yamamoto M, Ogawa S, Yagi S. XAFS analysis for quantification of the gallium Coordinations in Al_2O_3-supported Ga_2O_3 photocatalysts. *J Phys Conf Ser*. 2016;712(1):Article 012056.
24. Harada T, Ito S, Tsukazaki A. Electric dipole effect in $PdCoO_2$/β-Ga_2O_3 Schottky diodes for high-temperature operation. *Sci Adv*. 2019;5(10):eaax5733.
25. Han Z, Choi C, Hong S, Wu TS, Soo YL, Jung Y, Qiu J, Sun Z. Activated TiO_2 with tuned vacancy for efficient electrochemical nitrogen reduction. *Appl Catal B Environ*. 2019;257:Article 117896.
26. Tian Y, Liu X, Xu L, Yuan D, Dou Y, Qiu J, Li H, Ma J, Wang Y, Su D, et al. Engineering crystallinity and oxygen vacancies of co(II) oxide nanosheets for high performance and robust rechargeable Zn–air batteries. *Adv Funct Mater*. 2021;31(20):2101239.
27. Bagchi D, Raj J, Singh AK, Cherevotan A, Roy S, Manoj KS, Vinod CP, Peter SC. Structure-tailored surface oxide on cu–Ga

Intermetallics enhances CO_2 reduction selectivity to methanol at ultralow potential. *Adv Mater*. 2022;34(19):2109426.
28. Hejral U, Timoshenko J, Kordus D, Luna ML, Divins NJ, Widrinna S, Zegkinoglou I, Pielsticker L, Mistry H, Boscoboinik JA, et al. Tracking the phase changes in micelle-based NiGa Nanocatalysts for methanol synthesis under activation and working conditions. *J Catal*. 2022;405:183–189.
29. Sharma A, Varshney M, Shin HJ, Chae KH, Won SO. Investigation on cation distribution and luminescence in spinel phase γ-$Ga_{3-\delta}O_4$: Sm nanostructures using X-ray absorption spectroscopy. *RSC Adv*. 2017;7(83):52543–52554.
30. Cafferty BJ, Yuan L, Baghbanzadeh M, Rappoport D, Beyzavi MH, Whitesides GM. Charge transport through self-assembled monolayers of monoterpenoids. *Angew Chem Int Ed*. 2019;58(24):8097–8102.
31. Isomura N, Kikuta D, Takahashi N, Kosaka S, Kataoka K. Local atomic structure analysis of GaN surfaces *via* X-ray absorption spectroscopy by detecting auger electrons with low energies. *J Synchrotron Radiat*. 2019;26(Pt 6):1951–1955.
32. Lichterman MF, Hu S, Richter MH, Crumlin EJ, Axnanda S, Favaro M, Drisdell W, Hussain Z, Mayer T, Brunschwig BS, et al. Direct observation of the energetics at a semiconductor/liquid junction by operando X-ray photoelectron spectroscopy. *Energy Environ Sci*. 2015;8(8):2409–2416.
33. Xiao Y, Xie K. Active exsolved metal–oxide interfaces in porous single-crystalline ceria monoliths for efficient and durable CH_4/CO_2 reforming. *Angew Chem Int Ed*. 2022;61(1):Article e202113079.
34. Batchu SP, Wang HL, Chen W, Zheng W, Caratzoulas S, Lobo RF, Vlachos DG. Ethane dehydrogenation on single and dual centers of Ga-modified α-Al_2O_3. *ACS Catal*. 2021;11(3):1380–1391.
35. Zhang K, Xu Z, Zhao J, Wang H, Hao J, Zhang S, Cheng H, Dong B. Anisotropies of angle-resolved polarized Raman response identifying in low miller index β-Ga_2O_3 single crystal. *Appl Surf Sci*. 2022;581:Article 152426.